

Magnetically Actuated Nanorod Arrays as Biomimetic Cilia

B. A. Evans,^{†,||} A. R. Shields,^{†,||} R. Lloyd Carroll,[‡] S. Washburn,^{†,§}
M. R. Falvo,^{†,§} and R. Superfine^{*,†,§}

The Virtual Lung Project, Department of Physics and Astronomy, University of North Carolina at Chapel Hill, Chapel Hill, North Carolina 27599, Department of Chemistry, West Virginia University, Morgantown, West Virginia 26506, and Curriculum in Applied and Materials Sciences, University of North Carolina at Chapel Hill, Chapel Hill, North Carolina 27599

Received January 24, 2007; Revised Manuscript Received March 16, 2007

Ⓜ This paper contains enhanced objects available on the Internet at <http://pubs.acs.org/nano>.

ABSTRACT

We present a procedure for producing high-aspect-ratio cantilevered micro- and nanorod arrays of a PDMS–ferrofluid composite material. The rods have been produced with diameters ranging from 200 nm to 1 μm and aspect ratios as high as 125. We demonstrate actuation of these superparamagnetic rod arrays with an externally applied magnetic field from a permanent magnet and compare this actuation with a theoretical energy-minimization model. The structures produced by these methods may be useful in microfluidics, photonic, and sensing applications.

High-aspect-ratio nanostructures have attracted increasing attention in the nanotechnology community due to their potential applications as sensors^{1–3} and actuators^{4–7} and the effect of their presence on the surface properties of a material such as adhesion^{8–11} and wetting.^{12–14} We are interested in producing high-aspect-ratio nanostructures to serve as biomimetic cilia for the purpose of studying the mechanics of nanoscale fluid flow in a ciliated system. To this end, we have produced soft polymeric, actuable nanostructures of the size of biological cilia ($\sim 10 \mu\text{m}$ in length by $\sim 200 \text{ nm}$ diameter.) High-aspect-ratio polymer rods have been produced with materials with elastic moduli on the order of 100 MPa,^{12–13} but these are unsuitable as actuating mechanisms due to their stiffness. Softer materials, such as poly(dimethyl siloxane) (PDMS, $E \sim 2 \text{ MPa}$), have been reported to fail at large aspect ratios due to lateral or ground collapse.^{15,16} In addition, in many cases, rodlike microstructures are fabricated via a photolithographic master^{15,16} or anodized aluminum oxide (AAO) membrane.¹⁷ However, conventional photolithographic molds involve lengthy or specialized processing to produce large arrays of upright high-aspect-ratio structures, and AAO membranes impose severe limits on the diameter and spacing of the pores. Furthermore, with soft materials, photolithographic lift-off procedures may lead

to structure collapse. Particle track-etched membranes have successfully been used as a template for a variety of materials^{18–20} and are able to produce high-aspect-ratio structures with variable spacing and diameter. We use polycarbonate track-etched (PCTE) membranes as templates, allowing us to freely select the length and diameter of the rods and the density of the rod array by choosing an appropriate membrane.

The high-aspect-ratio and low elastic modulus of our PDMS rods lend them a flexibility that makes them ideally suited to serve as actuators. To this end, we have produced micro- and nanorod arrays using a composite material of PDMS and iron oxide nanoparticles, which results in flexible superparamagnetic rods that may be actuated by applied external magnetic fields. Other groups have devised high-aspect-ratio magnetically actuated microstructures via linked-bead chains,^{3,7} and Singh, et al. have succeeded in tethering these structures to a substrate.⁶ Our templated structures do not necessarily require a liquid medium, have the advantage of being scalable beyond the limitations of commercially available magnetic beads and may have an easily tunable magnetic loading fraction. In addition, our templating method can be easily generalized beyond the production of rodlike structures to produce other useful formations.

In addition to fabricating these actuating structures, we have developed a theoretical model to predict their bending behavior in a given magnetic field geometry. Other groups have proposed mathematical models for the magnetic actuation of flexible high-aspect-ratio structures, but these models

* Corresponding author. E-mail: rsuper@physics.unc.edu.

[†] The Virtual Lung Project, University of North Carolina at Chapel Hill.

[‡] Department of Chemistry, West Virginia University.

[§] Curriculum in Applied and Materials Sciences, University of North Carolina at Chapel Hill.

^{||} These authors contributed equally to this work.

have been limited to structures in constant fields.^{3,21–23} Our experiments have shown that the magnetic field gradient can be dominant in influencing the behavior of cantilevered rod arrays, and so we have developed an energy-minimization model that describes the actuation of our nanorod arrays in a spatially varying magnetic field. We have validated this model by comparison with experiment.

The nanorods are composed of a composite material consisting of a homogeneous dispersion of an iron oxide-based ferrofluid in a polymer matrix. We produce a ferrofluid of magnetite nanoparticles (Fe_3O_4) suspended in water by coprecipitation of iron salts as described by Massart.²⁴ To increase the magnetic permeability of the ferrofluid, we then boil the Fe_3O_4 in an aqueous solution of iron nitrate to oxidize the nanoparticles and convert them to maghemite (Fe_2O_3).²⁵ In this manner, we have been able to produce stable aqueous solutions of up to 5% maghemite by weight. We convert the aqueous ferrofluid to an organic ferrofluid by extraction into neat oleic acid.²⁶ The resulting oleic acid-stabilized nanoparticles (after washing with ethanol to remove excess oleic acid) resuspend easily in organic solvents to form stable ferrofluids in hexane and toluene. Hexadecane is then added in a 1:1 v/v ratio to the oleic acid nanoparticle suspension and is further diluted in toluene (5:1 v/v toluene to product). The PDMS prepolymer (Dow Corning Sylgard 184) is also diluted 5:1 by volume with toluene. We then combine the diluted nanoparticle suspension and prepolymer over the course of several minutes under ultrasonication by a Fisher Scientific Sonic Dismembrator 550 operating at 150 W. We remove the toluene by rotational evaporation with a Büchi Rotovapor R110. Upon standing for several days, excess hexadecane separates from the composite, leaving behind a stable suspension of maghemite nanoparticles in a PDMS–hexadecane matrix. SQUID measurements of the resulting ferrofluid–PDMS composite (henceforth FFPDMS) show the saturation magnetization to be $12.6 \pm 0.2 \text{ A m}^2/\text{kg}$, indicating a maghemite loading of 18 wt % (4% vol.)

Rod arrays are fabricated by templating the FFPDMS composite in the pores of PCTE membranes and subsequently freeing the rod array by dissolving the template in an organic solvent. We obtained PCTE membranes commercially (it4ip s.a., rue Jules Bordet, 7180 Seneffe, Belgium) with pore diameters of 200 nm, membrane thicknesses of 10 and 25 μm , and a pore density of 2×10^6 pores/ cm^2 . We are able to increase the pore diameter by etching the membranes in a NaOH solution.²⁷ This allows us to produce rod arrays with pore diameters ranging from 200 nm to 1 μm .

Figure 1 summarizes the steps used to prepare the templated magnetically actuatable rod arrays. The membrane pores are impregnated with FFPDMS by immersion (Figure 1A), and the outer surfaces of the membrane are gently cleaned of excess FFPDMS. The impregnated membrane is then submerged in a small drop of uncured Sylgard 184 PDMS mixed 10:1 with curing agent and placed directly on a no. 1.5 glass coverslip in the center of a $\sim 100 \mu\text{m}$ thick PDMS well that has been permanently sealed to the glass

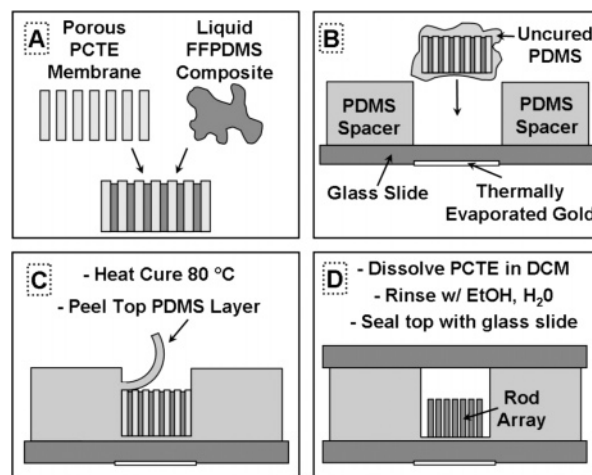


Figure 1. Cross-sectional view of the fabrication steps used to template magnetically actuated composite polymer rod arrays. Details in the text.

(Figure 1B). The sample is then placed in a convection oven at 80 °C for several hours to cure.

Upon removal from the oven, the upper layer of encapsulating PDMS is carefully peeled away to expose the polycarbonate membrane (Figure 1C). Once exposed, the membrane is dissolved in a 60 °C bath of dichloromethane (DCM) for about 10 min. The sample is gently rinsed with clean DCM, followed by ethanol to remove the dissolved membrane. A no. 0 coverslip is then placed on top of the PDMS spacer and sealed with Norland optical adhesive no. 81 to prevent evaporation of the ethanol.

Using this method, we have succeeded in fabricating and actuating rod arrays as small as biological cilia ($\sim 200 \text{ nm}$ diameter and $\sim 10 \mu\text{m}$ length), and with aspect ratios as high as 125 ($\sim 200 \text{ nm}$ diameter and $\sim 25 \mu\text{m}$ length) in liquid media. To actuate rod arrays in air, they must first be dried via critical-point drying with CO_2 (Balzers Union CPD 020). However, only rod arrays with diameters larger than $\sim 500 \text{ nm}$ (aspect ratios < 50) have survived the drying process without complete collapse, as demonstrated in the scanning electron micrographs seen in Figure 2. Previous work^{15,16} has shown that the collapse of similar structures with low Young's moduli and high aspect ratios is due to surface adhesive forces between neighboring structures (lateral collapse) or between the rod structures and the substrate (ground collapse). The aspect ratio at which structures become susceptible to collapse depends on the work of adhesion of the material, which in turn is a function of the medium surrounding the structures. Thus, the failure of our smallest diameter rod arrays to survive drying is most likely caused by the increase in the work of adhesion of the PDMS in air versus ethanol or water. In future work, we hope to chemically modify the surface of the PDMS to decrease the likelihood of collapse. However, with current fabrication methods, our rod arrays are never exposed to air. This prohibits us from using an oxygen plasma to chemically activate the PDMS surface prior to modification, which is the typical method of surface modification reported in the literature.²⁸

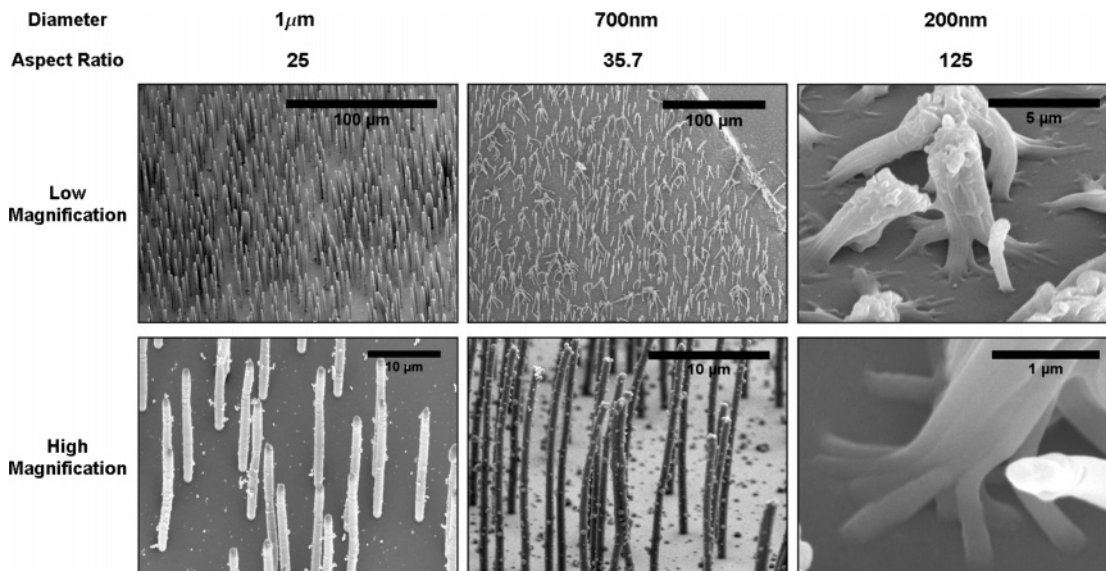


Figure 2. SEM images of various diameters of magnetically actuated rod arrays after being dried using supercritical CO_2 . In liquid environments, we are able to reliably fabricate and actuate rod arrays in the range of diameters pictured. However, as the diameter decreases, the rods become very flexible and supercritical drying without substantial rod collapse becomes increasingly difficult.

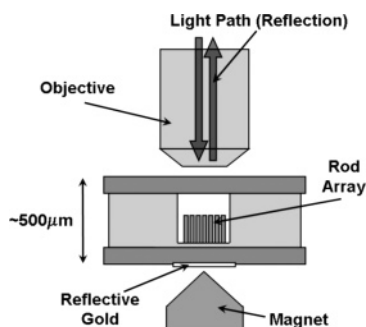


Figure 3. Experimental setup used to magnetically actuate rod arrays with simultaneous optical imaging. The thickness of the entire sample has been reduced to $500 \mu\text{m}$ to allow high magnification microscopy from above while applying large magnetic forces from below.

The actuation of the rod arrays is induced via an externally applied magnetic field produced by neodymium-iron-boride (NIB) permanent magnets. Simultaneous optical imaging of the rod arrays is performed using the reflectance mode of a Leitz Wetzlar microscope. The reflectance mode allows a permanent magnet to be inserted immediately beneath the array (opposite the objective) to provide maximum magnetic forces without interfering with the optical path, as pictured in Figure 3. Reducing the total thickness of the sample (coverslip to coverslip, inclusive) to just $400 \mu\text{m}$ allows us to position the actuating magnet within $250 \mu\text{m}$ of the rod array from below while facilitating observation with high-magnification short-working-distance objectives from above. At $250 \mu\text{m}$ above the magnet, the rod arrays may be subjected to magnetic fields and field gradients as large as 0.5 T and 500 T/m , respectively.

With $25 \mu\text{m}$ tall rods, our permanent magnet assemblies can generate rod tip displacements of at least $7 \mu\text{m}$, which corresponds to a bending angle of 20° . We define the bending

angle as the angle between the vertical and the line connecting the base of the rod with the tip. This is calculated by measuring the displacement of its tip relative to its base and using the known height of the rod. However, across any given sample, we usually observe substantially different bending angles, even between rods in close proximity. This is attributable to any number of factors such as variations in the strength of the connection between rod base and substrate, the concentration of magnetic material in a given rod, or the degree of polymer cross-linking in the rod.

Once fabricated, we can induce a variety of rod beat patterns by moving the magnet underneath the rod array. We have been able to actuate in these patterns at frequencies of $\sim 15 \text{ Hz}$, which is the approximate beating frequency of human airway epithelial cilia. Two examples of actuation strokes can be seen in Figure 4, where single 500 nm diameter rods are displayed undergoing linear or back-and-forth (Figure 4A) and rotational (Figure 4B) actuation. The linear stroke is similar to the beat pattern of human airway cilia, while the rotational stroke is much like that of embryonic nodal cilia.²⁹ An array of rods also exhibiting rotational actuation is pictured in Figure 5. The flexibility to engineer specific rod beat patterns at a variety of frequencies plays an integral role in current and future work to investigate the fluid flow that is induced by the actuation of our rod array.

Our goal is to be able to design rod arrays and magnetic field geometries to generate a variety of spatial and temporal beat patterns. To this end, we have developed an energy minimization model of a flexible magnetic rod in the presence of a defined magnetic field and field gradient. A model for the energy of a flexible magnetic rod in a homogeneous magnetic field has been proposed by multiple authors.^{3,21–23} However, because our experimental results are not consistent with a gradient-free field, we have developed

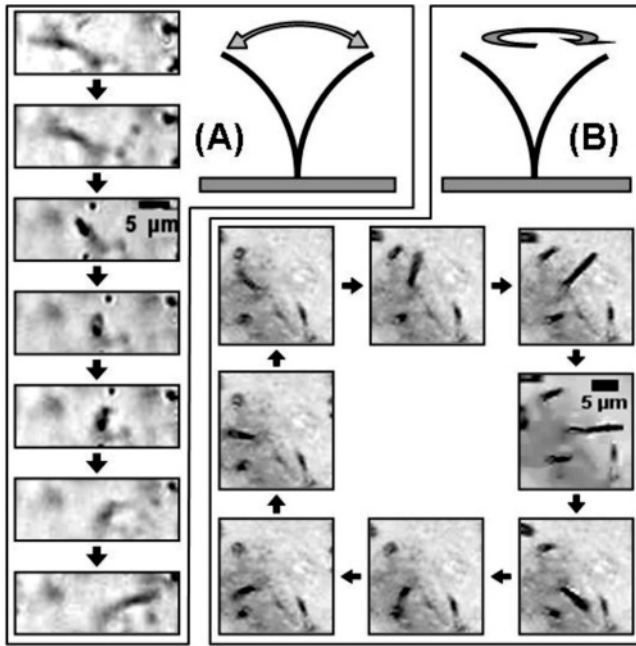


Figure 4. (A) Linear and (B) rotational actuation strokes of a single 500 nm rod with aspect ratio 50. Engineering specific magnetic geometries allows for a variety of rod beat patterns to be executed.

Ⓜ View the web enhanced objects (.mov) for Ⓜ (A) and Ⓜ (B) for videos of these actuation strokes.

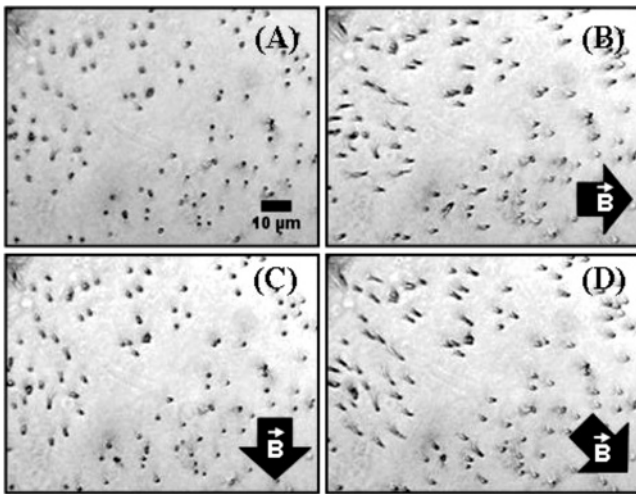


Figure 5. Rotational actuation of an array of 500 nm diameter rods with aspect ratios of 50. In (A), the rod array is pointing straight up, while in (B), (C), and (D), the arrows represent the planar direction of the applied magnetic field. Only about 0.1% of the entire sample array can be seen in these images. See Supporting Information for video (.mov) of the array actuation.

a model that is able to account for the effects of both a magnetic field and a magnetic field gradient on a cantilevered, flexible magnetic rod. We conclude that the effect of a torque applied by a magnetic field may be dominated by the effect of a force caused by a magnetic field gradient.

The total energy of the magnetic rod system is given by $U_T = U_E + U_M$, where U_E is the elastic energy of the bent rod and U_M is the magnetic energy of the rod in an applied

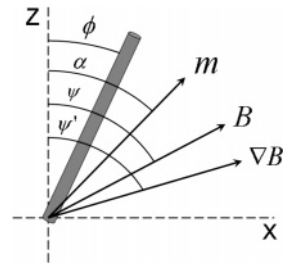


Figure 6. Angle and vector definitions used in deriving the rod bending theory. B is the applied magnetic field, ∇B is the applied field gradient, and m is the rod's magnetic moment.

magnetic field. The elastic energy is described by the Kirchhoff model of a uniform elastic rod³⁰ and has the form

$$U_E = \frac{1}{2} EI \int_0^L \frac{1}{R(s)^2} ds \quad (1)$$

where E is the Young's modulus of the rod, I is the bending moment ($I = \pi/4 r^4$ for a rod of circular cross-section), and $R(s)$ is the radius of curvature of the bent rod. In this work, we do not solve for the shape of the rod in an applied field but assume a constant curvature, and hence set $R(s) = R$. We therefore set $R = L/2\phi$ (see Figure 6), and the elastic energy can be written as $U_E = (\pi/2)(Er^4/L)\phi^2$. From more complete calculations of the rod bending energy, we estimate that the constant curvature assumption introduces an error of less than 30%.

In general, the magnetic energy contained in a rod can be described by the following integral,

$$U_M = -A \int_0^L \vec{B}_T(s) \cdot \vec{M}(s) ds \quad (2)$$

where A is the cross-sectional area of the rod, $\vec{M}(s)$ is the magnetization at a point along the length of the rod and the total field $\vec{B}_T = \vec{B}_N + \vec{B}_I + \vec{B}_A$, where \vec{B}_N , \vec{B}_I , and \vec{B}_A are the magnetic field from neighboring rods, the internal magnetic field, and the applied external magnetic field, respectively. In this sense, the total magnetic energy can be thought of as a sum of three energies, one for each of the component fields.

$$U_M = U_N(B_N) + U_I(B_I) + U_A(B_A) \quad (3)$$

We can show that the field produced by nearest-neighbor rods is negligible compared to the magnitude of the applied field, so the first term will be ignored. The second term, the internal magnetic energy of the rod, has been described by Stoner–Wohlfarth for an ellipsoid of revolution.³¹

$$U_I = \frac{1}{2} \mu_0 \frac{m^2}{V} (N_a - N_b) \cos^2(\alpha - \phi) \quad (4)$$

Here α and ϕ are the angular positions of the net magnetic moment of the rod, m , and the long axis of the rod, respectively, from the vertical (Figure 6). In the Stoner–Wohlfarth model, N_a and N_b are the demagnetization factors

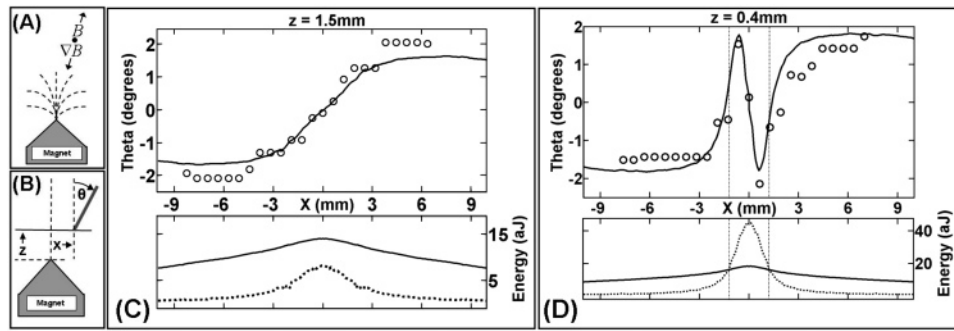


Figure 7. (A) Diagram of magnetic field lines from the steel-tipped magnet used in these experiments. (B) Definition of rod and field geometries. (C,D) Graphs of rod bending angle (top) and magnetic energies (bottom) vs magnet tip position (X) at a constant z . For both (C) and (D), in the upper plot, the open circles are the experimentally observed average bending and the solid line is the theoretically predicted bending. When the magnet's tip is within $z \sim 0.5$ mm (D), there is a rapid switching of the rod orientation as it passes over the tip. Our theoretical calculations suggest that, at distances closer to the magnet, the gradient energy (dashed lines) becomes larger than the field energy (solid lines), causing the rods to bend away from the field lines.

Ⓜ For video of these actuation patterns in Ⓜ (C) and Ⓜ (D), see the web enhanced objects (.mov).

along the long axis of the rod and along the radius of the rod, respectively, and V is the volume of the rod. For a rod of aspect ratio greater than 20, as is satisfied by our experiments, $N_a \sim 0$ and $N_b \sim 0.50$. In addition, it can be shown that, under the condition $4B/[\mu_0 M(B)f] \gg 1$, which is satisfied by our experiments, the magnetic moment of the rod aligns with the applied magnetic field (see Appendix for details). We can therefore replace α with ψ , the angular position of the applied field with respect to the vertical. The internal magnetic energy for a straight rod then becomes

$$U_I = -\frac{1}{4}\mu_0 \frac{m^2}{V} \cos^2(\psi - \phi) \quad (5)$$

The third magnetic energy term, the energy due to the applied field, may be written as follows (see Appendix for derivation and other details).

$$U_A = -\frac{1}{2}m\nabla B L \cos(\psi' - \phi) \quad (6)$$

where ψ' is the angular position of the magnetic field gradient with respect to the vertical (Figure 6). We can now write down the total energy of the rod, elastic, and magnetic.

$$U_T = \frac{\pi Er^4}{2L} \phi^2 - \frac{1}{4}\mu_0 \frac{m^2}{V} \cos^2(\psi - \phi) - \frac{1}{2}m\nabla B L \cos(\psi' - \phi) \quad (7)$$

In general, the magnetic moment $m = M(B)Vf$, where $M(B)$ is the magnetization of the magnetic particles in the rod and f is the volume fraction of magnetic material. In our model, the magnetization curve $M(B)$ is determined by SQUID measurements of the maghemite, allowing us to determine the magnetic moment m for any applied field.

At this point, it is evident that the third term in the total energy does not depend on the magnetic field directly, but only on the magnetic field gradient. This term represents

the effect of the gradient pulling on the center of mass of the bent rod, which we will call "gradient energy." The second term in the total energy depends on the direction of the magnetic field and will be called "field energy." The field energy term represents the misalignment of the long axis of the rod from the direction of the applied field.

The energy function can be applied to a specific magnetic field geometry to determine the angular position of the rods at any point in space. We use a finite element modeling software (COMSOL Multiphysics) to generate a model of the magnetic field geometry created by the conical actuating magnet, allowing us to determine the field and field gradient at any position with respect to the actuating magnet. We adjust the physical parameters of the COMSOL model to match measured values of the magnetic field along the axis of the cone tip (measured by a F.W. Bell Model 5080 G/Teslameter). The magnetic field, B , magnetic field gradient, ∇B , and the angles of each with respect to the vertical, ψ and ψ' , at a particular rod position, are then passed to MatLab 7.1, which minimizes the total energy function for the given field and gradient with respect to ϕ . The ϕ that minimizes the total energy is output as the final angular position of the rod.

We performed an actuation experiment in which a magnet was moved beneath the sample while under observation by optical microscopy (as described above and pictured in Figure 3). The magnet was comprised of two cylindrical neodymium iron boride (NIB) magnets (25 mm diameter, 6 mm height) topped with a cone of 12L14 steel. This produced a field in the region above the magnet (see Figure 7A) in which the magnetic field and the field gradient point in opposing directions. In addition, the steel tip focuses the field lines and produces a particularly large gradient near the tip of the cone.

This steel-tipped magnet was translated beneath the rod array at a distance z below the rods. The plots in Figure 7 show the average angle through which the rods are bent as a function of the rod position relative to the magnet tip for two different heights above the magnet. To obtain the

theoretical fit displayed in each plot, we used an algorithm written in MatLab to minimize the root-mean-square deviations between the theoretical and experimental curves with respect to the physical parameters f , E , r , and L . Because the experimental data in the following two plots represent the same rods at different heights above the magnet, the root-mean-square deviations of both sets of curves were minimized simultaneously with respect to the same set of parameters.

According to the minimization routine, a Young's modulus of 2.6 MPa best fit the experimental data shown in Figure 7. The literature suggests a Young's modulus of 2.3–2.7 MPa for Sylgard 184 PDMS with a 1:10 curing agent to prepolymer ratio.³² Work by Guild and Young³³ suggests that the small amount of maghemite nanoparticles in our FFPDMS rods ($\sim 4\%$ by volume) should have little effect on the Young's modulus of the material.

The upper limit for the volume fraction of maghemite loading in our rods was taken to be 4%, as indicated by SQUID measurements on a bulk sample of FFPDMS. However, the actual fraction of maghemite in the templated rods may be significantly lower due to dilution of the material with hexadecane during processing, possible exclusion of maghemite aggregates from the pores, or dilution of the FFPDMS due to diffusion of PDMS and curing agent into the pores just before curing. The minimization routine returned a value of 1.4%, which is consistent with our expectations.

We have measured the radii and lengths of multiple rods in SEM micrographs of rods produced by the templates used in our experiments and have found the radii to be 125 ± 25 nm and the lengths to be $22.5 \pm 2.5 \mu\text{m}$. The $21 \mu\text{m}$ length and 136 nm radius returned by the minimization routine fall well within these ranges.

The optimized model fit and the experimental bending data are shown in Figure 7. A novel feature of these experiments which cannot be predicted by a constant field model is exhibited in Figure 7D. In this example, the positive angles exhibited at large distances to the right of the magnet (and negative values exhibited at large distances to the left) indicate an alignment of the rods with the magnetic field of the conical tip and therefore a tendency to point away from the magnet. This behavior occurs in areas of large field energy and small gradient energy. Closer to the magnet, however, the field gradient becomes large enough to overwhelm the field alignment effect, and the rods are pulled by the gradient toward the magnet tip (shown in the large negative angles immediately to the right of $X = 0$, and large positive angles to the left.) We have seen this behavior in planes very close to the tip of the magnet (less than $\sim 500 \mu\text{m}$), where the gradient is able to dominate, and not at greater heights above the magnet.

In summary, we have developed a technique for producing large arrays of high-aspect-ratio nanostructures of tunable dimensions. The technique enables the use of softer structural materials than are feasible through other methods, facilitating the fabrication of highly responsive sensors and actuators. We have produced a novel magnetic–polymeric composite

material, which we have used in conjunction with our templating techniques to fabricate high-aspect-ratio magnetically actuated rod structures, and have demonstrated the actuation of these structures in applied magnetic fields. In addition, we have developed a theoretical model which describes the motion of the rods in applied magnetic fields and will allow us to gain better control over the mode of actuation of our rod arrays and inform our design processes in future experiments. We believe structures and control produced by the methods outlined above may be useful in microfluidics, photonic, and sensing applications. In addition, we have experimentally demonstrated fluid flow induced by beating rod arrays and will present details in future publications.

Acknowledgment. This work was supported by NASA-URETI (NCC-1-02037), NIH (P41-EB002025-23A1 and RO1-EB000761), NSF-NIRT (CMS-0507151), NSF-RTG (DMS-0502266), and the National Heart, Lung, and Blood Institute (R01-HL077546-01A2)

Supporting Information Available: Video (.mov) of 500 nm diameter rod actuation modes displayed in Figure 5. This material is available free of charge via the Internet at <http://pubs.acs.org>.

Appendix

Taking a look for a moment at the case of a rigid rod in a constant magnetic field, we could quickly write down the total magnetic energy as the sum of this internal energy and the energy from an applied field ($\vec{m} \cdot \vec{B}$) as follows:

$$U'_T = -\frac{1}{4}\mu_0 \frac{m^2}{V} \cos^2(\alpha - \phi) - mB \cos(\psi - \alpha) \quad (8)$$

The second term dominates if $4B/[\mu_0 M(B)f] \gg 1$ (where we have used the fact that $m = M(B)Vf$, where $M(B)$ is the magnetization curve of the magnetic material in the rod and f is the volume fraction of magnetic material in the composite), and the energy is therefore minimized when the magnetic moment lies along the field line ($\psi = \alpha$). This condition depends only on the material and not the geometry of the rod. For our material, where $M(B)$ is the magnetization curve of the maghemite as determined by SQUID measurements, $4B/[\mu_0 M(B)f] \sim 100$. We may therefore assume that the magnetic moment of the rod aligns at every point along the length of the rod with the applied magnetic field, i.e., that \vec{B}_A and $\vec{M}(B)$ are parallel.

With this in mind, the third term (the energy of the rod in an applied external field) can be written as follows

$$U_A = -A \int_0^L B_A M(B) dl \quad (9)$$

Because B_A is nonuniform, we can approximate it with the first couple terms of a Maclaurin series as follows:

$$B(l) = B_0 + \nabla B l \cos(\psi' - \phi) + 2l^2 \frac{\partial}{\partial l}(\nabla B) + \dots \quad (10)$$

For our experiments, $l \sim 25 \mu\text{m}$, $\nabla B \sim 300 \text{ T/m}$, and $\partial/\partial l(\nabla B) \sim 3 \times 10^5 \text{ T/m}^2$. Therefore the third term of the expansion is approximately 20 times smaller than the second and may be ignored.

The magnetization of the material, $M(B)$ depends on the applied magnetic field in a rather complicated manner, as described by the hysteresis curve of the material. For fields that are small enough that they do not saturate the material, however, we can approximate the magnetization as linear with respect to magnetic field, $M(B) = \chi B(l)$. Inserting these relationships into the applied field energy term from above,

$$U_A = -A\chi \int_0^L [B_0 + \nabla B l \cos(\psi' - \phi)]^2 dl \quad (11)$$

Because of the extremely small size of the nanorods in our experiments, $B \gg \nabla B l$ (for our experimental geometries, $B/\nabla B l \sim 100$), and upon squaring, the term of order $(\nabla B l)^2$ can be ignored. Thus, after integrating,

$$U_A = AL\chi B_0 \left[B_0 + \frac{1}{2} \nabla B L \cos(\psi' - \phi) \right] \quad (12)$$

The first term is constant with respect to the motion of the rod and may be dropped. Recognizing that $AL\chi B_0 = m$, the magnetic moment of the rod, the applied field term becomes

$$U_A = \frac{1}{2} m \nabla B L \cos(\psi' - \phi) \quad (13)$$

For larger fields, we can arrive at the same result by assuming that, as the metal approaches saturation, we can approximate the magnetization as constant with respect to field, $M(B) = M$. Inserting a constant magnetization and the first two terms of the Maclaurin series (eq 10) into eq 9, we again obtain the energy U_A derived above.

This term can be thought of as the effect of the magnetic field gradient pulling on a magnetic moment of magnitude m located at the centroid of the rod. Under the straight-rod assumption of the Maclaurin series, the centroid is located on the long axis of the rod, half way along its length. For a rod of constant curvature, however, the centroid does not lie on the axis of the rod. By geometrical arguments, we can show that, for a rod bent through an angle $\leq 90^\circ$, the error in the position of the centroid generated by the straight rod assumption is $\sim 33\%$. Given that the field gradient is

approximately linear on the scale of the rods, this results in an error of $\leq 33\%$ in this term.

References

- (1) Engel, J. M.; Chen, J.; Liu, C.; Bullen, D. *J. Microelectromech. Syst.* **2006**, *15*, 729–736.
- (2) McGary, P. D.; Tan, L. W.; Zou, J.; Stadler, B. J. H.; Downey, P. R.; Flatau, A. B. *J. Appl. Phys.* **2006**, *99*, 08B310.
- (3) Goubault, C.; Jop, P.; Fermigier, M.; Baudry, J.; Bertrand, E.; Bibette, J. *Phys. Rev. Lett.* **2003**, *91*, 260802.
- (4) Judy, J. W.; Muller, R. S. *Sens. Actuators, A* **1996**, *53*, 392–397.
- (5) Tabata, O.; Hirasawa, H.; Aoki, S.; Yoshida, R.; Kokufuta, E. *Sens. Actuators, A* **2002**, *95*, 234–238.
- (6) Singh, H.; Laibinis, P. E.; Hatton, T. A. *Nano Lett.* **2005**, *5*, 2149–2154.
- (7) Furst, E. M.; Suzuki, C.; Fermigier, M.; Gast, A. P. *Langmuir* **1998**, *14*, 7334–7336.
- (8) Sitti, M.; Fearing, R. S. *J. Adhes. Sci. Technol.* **2003**, *17*, 1055–1073.
- (9) Glassmaker, N. J.; Jagota, A.; Hui, C. Y.; Kim, J. J. *R. Soc. Interface* **2004**, *1*, 23–33.
- (10) Hui, C. Y.; Glassmaker, N. J.; Tang, T.; Jagota, A. *J. R. Soc. Interface* **2004**, *1*, 35–48.
- (11) Glassmaker, N. J.; Jagota, A.; Hui, C. Y. *Acta Biomaterialia* **2005**, *1*, 367–375.
- (12) Oner, D.; McCarthy, T. J. *Abstr. Pap. Am. Chem. Soc.* **2000**, *220*, U270–U271.
- (13) Feng, L.; Li, S. H.; Li, Y. S.; Li, H. J.; Zhang, L. J.; Zhai, J.; Song, Y. L.; Liu, B. Q.; Jiang, L.; Zhu, D. B. *Adv. Mater.* **2002**, *14*, 1857–1860.
- (14) Fan, J. G.; Tang, X. J.; Zhao, Y. P. *Nanotechnology* **2004**, *15*, 501–504.
- (15) Roca-Cusachs, P.; Rico, F.; Martinez, E.; Toset, J.; Farre, R.; Navajas, D. *Langmuir* **2005**, *21*, 5542–5548.
- (16) Zhang, Y.; Lo, C. W.; Taylor, J. A.; Yang, S. *Langmuir* **2006**, *22*, 8595–8601.
- (17) Chik, H.; Xu, J. M. *Mater. Sci. Eng., R* **2004**, *43*, 103–138.
- (18) Schonenberger, C.; vanderZande, B. M. I.; Fokkink, L. G. J.; Henny, M.; Schmid, C.; Kruger, M.; Bachtold, A.; Huber, R.; Birk, H.; Staufner, U. *J. Phys. Chem. B* **1997**, *101*, 5497–5505.
- (19) Hulsteen, J. C.; Martin, C. R. *J. Mater. Chem.* **1997**, *7*, 1075–1087.
- (20) Brumlik, C. J.; Menon, V. P.; Martin, C. R. *J. Mater. Res.* **1994**, *9*, 1174–1183.
- (21) Cebers, A. *Curr. Opin. Colloid Interface Sci.* **2005**, *10*, 167–175.
- (22) Cebers, A.; Javaitis, I. *Phys. Rev. E* **2004**, *70*, 021404.
- (23) Shcherbakov, V. P.; Winklhofer, M. *Phys. Rev. E* **2004**, *70*, 061803.
- (24) Massart, R. *IEEE Trans. Magn.* **1981**, *17*, 1247–1248.
- (25) Bee, A.; Massart, R.; Neveu, S. *J. Magn. Mater.* **1995**, *149*, 6–9.
- (26) van Ewijk, G. A.; Vroege, G. J.; Philipse, A. P. *J. Magn. Mater.* **1999**, *201*, 31–33.
- (27) Ferain, E.; Legras, R. *Nucl. Instrum. Methods Phys. Res., Sect. B* **1997**, *131*, 97–102.
- (28) Makamba, H.; Kim, J. H.; Lim, K.; Park, N.; Hahn, J. H. *Electrophoresis* **2003**, *24*, 3607–3619.
- (29) Nonaka, S.; Tanaka, Y.; Okada, Y.; Takeda, S.; Harada, A.; Kanai, Y.; Kido, M.; Hirokawa, N. *Cell* **1999**, *99*, 116.
- (30) Landau, L. D.; Lifshitz, E. M. *Theory of Elasticity*, 3rd ed.; Pergamon Press: New York, 1986.
- (31) Stoner, E. C.; Wohlfarth, E. P. *Philos. Trans. R. Soc. London, Ser. A* **1947**, *240*, 559–642.
- (32) Gray, D. S.; Tien, J.; Chen, C. S. *J. Biomed. Mater. Res., Part A* **2003**, *66*, 605–614.
- (33) Guild, F. J.; Young, R. J. *J. Mater. Sci.* **1989**, *24*, 298–306.

NL070190C